Soft Matter

COMMUNICATION

View Article Online
View Journal | View Issue

Cite this: *Soft Matter*, 2024, **20**, 2212

Received 14th December 2023,
Accepted 7th February 2024

DOI: 10.1039/d3sm01699d

rsc.li/soft-matter-journal

Using cryo-SEM and EDS to investigate the stabilisation of oil–water interfaces in mixed aqueous-and-oil foams†

Yuchen Si, [a] Fraser H. J. Laidlaw, [a] Tao Li [b] and Paul S. Clegg *[a]

For multi-phase soft matter systems, optical microscopy is frequently employed to distinguish the different phases. Unfortunately, optical microscopy does not succeed in all cases. Consequently, researchers sometimes require more advanced imaging techniques with superior resolution or sample penetration capabilities. One such complex system is a mixed aqueous-and-oil foam stabilised by colloidal particles, which is composed of two immiscible foams organised as the dispersed and continuous phases of an emulsion. While its morphology has been extensively studied using fluorescence confocal microscopy, not all questions have been answered. While the aqueous phase bubble interfaces are stabilised by silica particles and the oil phase bubble interfaces are stabilised by fluorinated particles, it remains to be seen how the aqueous–oil interfaces are stabilised. Hence, to gain insights into the role of the different particles at the interfaces, we employ cryogenic scanning electron microscopy (Cryo-SEM) and energy-dispersive X-ray spectroscopy (EDS). We find that the hydrophobic silica particles reside at both the aqueous–air and aqueous–oil interfaces. In contrast, the fluorinated particles, which exhibit hydrophobic and oleophobic properties simultaneously, are exclusively found at the oil–air interfaces.

Emulsions and foams are versatile and essential components in, for example, food and drink, pharmaceutical formulations, oil recovery, and skincare and cosmetic products, and for environmental remediation.[1–3] The energy cost of the large amount of internal fluid–fluid interface demands the use of surfactants, proteins, polymers or solid particles to maintain their stability.[4–7] Colloidal particles are very effective interfacial stabilisers. They have been explored extensively as stabilisers of liquid droplets (in Pickering emulsions) and for stabilising bubbles in particle-stabilised foams.[8–10] In both cases, the colloidal particles create a barrier layer, which hinders coalescence. In foams, the particles can also play a role in reducing drainage.

Colloidal particles become trapped at fluid–fluid interfaces because they reduce the shared area between the immiscible fluids. This effect is maximized when the three-phase contact angle is close to 90°. Adjusting this contact angle can be achieved through various means, such as altering the particle surface chemistry,[11] solution pH,[12] particle shape,[13] particle roughness,[13,14] and liquid polarity.[15,16] Instabilities in droplets or bubbles often arise when the three-phase contact angle approaches 0° or 180° *i.e.* the colloidal particles exhibit a pronounced affinity for one of the immiscible fluids.[5,15,17,18]

We have previously created a novel multi-phase system by combining a particle-stabilised aqueous foam with a particle-stabilised oil foam.[19,20] The internal morphology of these mixed foams is that of an emulsion with bubbles in both phases. The two constituent foam systems, each requiring very different particles, have previously been studied in detail by others.[18,21,22] Mixed foams are different to the composites known as foamed emulsions,[23,24] which only include bubbles in the continuous phase. Our mixed foams are also distinct from capillary foams although these also use particle-stabilisation and contain two immiscible liquids.[25] In capillary foams, small amounts of oil form capillary bridges between bubbles radically changing the flow properties. In our previous research, fluorescence confocal microscopy and rheology were used to study the morphology and flow properties of mixed foams.[20] These studies revealed long-term stability and the emulsion-like morphology. Evidently, the samples contain large amounts of oil–water interfaces. In bulk samples we were unable to determine how these interfaces were stabilised.

In common with emulsions, mixed foams undergo inversions in which an oil-in-water (O/W) system becomes a water-in-oil (W/O) system or *vice versa*.[15,26–29] For particle-stabilised emulsions, transitional phase inversion can be driven by alterations in the hydrophobicity of the particles.[30] Catastrophic phase inversion is an alternative type of emulsion phase inversion that is primarily driven by changes in the proportions of

[a] *School of Physics and Astronomy, University of Edinburgh, Peter Guthrie Tait Road, Edinburgh, EH9 3FD, UK. E-mail: paul.clegg@ed.ac.uk*
[b] *Wenzhou Institute, University of Chinese Academy of Sciences, Wenzhou, Zhejiang, 325001, P. R. China*

† Electronic supplementary information (ESI) available. See DOI: https://doi.org/10.1039/d3sm01699d

the two phases.[27,31] In mixed-foams, transitional inversion is driven by altering the proportion of propylene glycol in the aqueous phase.[20] This changes the polarity of the aqueous phase and, by implication, the three-phase contact angle of any particles on the aqueous–oil interfaces. This tends to indicate that these interfaces are being stabilised by particles of some sort. In this paper, through a combination of cryo-SEM and EDS analysis, we investigate whether either of the particles functioning as foaming agents is also important for the stability of aqueous–oil interfaces. Cryo-SEM has previously been used to study complex multi-phase systems incorporating air, for example, ice cream.[32] Our research indicates that the inclusion of EDS analysis allows component distinguishability within a complex multi-phase system.

As outlined, the highly stable particle-stabilised aqueous and oil foams, each exhibiting a yield stress, can be mixed to form a stable mixed foam that unites the two immiscible liquids. The aqueous foams (Fig. 1(a)–(d)) are a blend of water and propylene glycol stabilised by hydrophobic silica particles (R972), while the oil foams (Fig. 1(e) and (f)) consist of olive oil stabilised by partially fluorinated particles (MP-8T). The detailed component information and preparation method are given in our previous work.[20] The confocal micrographs in Fig. 1 depict the aqueous phase in green and the oil phase in purple. These mixed foams are essentially emulsions in which both the dispersed and continuous phases themselves take the form of foams. Their characteristics are primarily influenced by the volume fraction of propylene glycol within the aqueous phase and the proportions of the aqueous and oil foams. The W/O mixed foams (Fig. 1(m) and (n)) are stable for more than a week, and the O/W samples are slightly less stable (Fig. 1(g)–(j)), whereas phase-separated samples (Fig. 1(k) and (i)) further separate within a week. The droplet size in the O/W samples is much larger than that in the W/O samples. The catastrophic phase inversion happens rapidly as the quantities of the dispersed phase increase. By contrast, the transitional phase inversion is a much slower process, and an intermediate phase-separated state that contains substantial oil and aqueous foam regions can be observed. The average bubble size of aqueous foam reaches a minimum when the propylene glycol and water composition is evenly divided by volume; meanwhile, the bubble number per unit area reaches a maximum (Fig. 1(a)–(c)). Therefore, for the O/W samples in Fig. 1(g) and (i), the sample with higher propylene glycol concentration (Fig. 1(g)) contained fewer aqueous bubbles. Because the oil foam and its corresponding fluorinated particles remained consistent throughout the experiment, the transitional phase inversion was assumed to be entirely caused by the change in wettability of the silica particles that stabilised the aqueous foams. The roles silica and fluorinated particles play at the oil–aqueous interface remain an open question.

Previous confocal microscopy studies of the mixed foam in thin-film form[19] showed evidence that the silica particles stabilise the liquid–liquid interfaces. Below, the nature of the oil–aqueous interfaces in bulk mixed foams is explored by a combination of cryo-SEM and EDS analysis. The cryo-SEM instrument used in this research was a Zeiss Crossbeam 550 FIB-SEM with a cryogenic attachment (Quorum Technologies). A gas-cooled cryo-preparation system (Quorum PP3010) was used to prepare the cryo-SEM samples. Initially, the sample was carefully scooped out and dropped on the brass rivet eyelet, a containment and conductive element to achieve fast freezing.

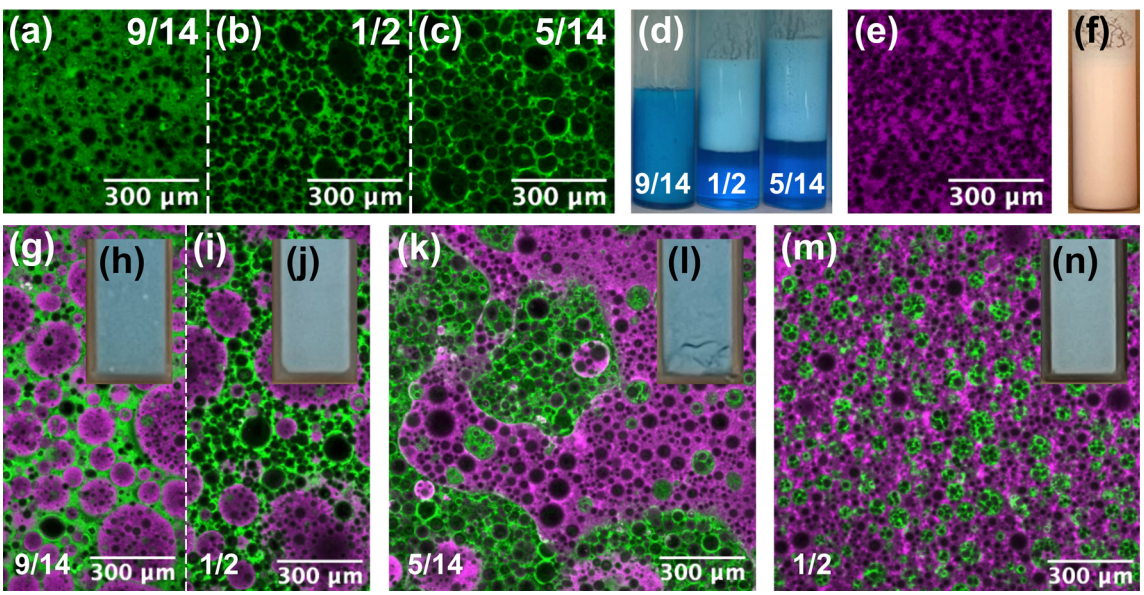

Fig. 1 By mixing (a)–(d) Nile blue-dyed aqueous foams (propylene glycol volume fractions are labelled) and (e) and (f) Nile red-dyed oil foams, the mixed foams can be (g)–(j) O/W, (k) and (l) phase-separated, and (m) and (n) W/O depending on the propylene glycol concentration and the foam proportions. (a)–(c), (e), (g), (i), (k) and (m) In the confocal micrographs, oil (20 wt% MP-8T particles in olive oil) and aqueous foams (3.0 wt% R972 particles in a mixture of propylene glycol and water) are coloured purple and green, respectively, for clarity. (d), (f), (h), (j), (l) and (n) Samples in bulk form. The aqueous to oil foam mass ratios are (g)–(l) 1 : 1, and (m) and (n) 2 : 3. The propylene glycol volume fractions in the aqueous phases are (g), (h) 9/14, (i), (j), (m) and (n) 1/2 and (k) and (l) 5/14.

Then, the sample was frozen rapidly by plunge freezing into slush nitrogen, ensuring that ice crystals formed in a controlled manner. Compared with freezing the sample under high pressure, nitrogen cooling tends to retain bubbles in the samples. Subsequently, under vacuum conditions, the frozen sample was transferred to the cryo-preparation chamber for cold fracturing and sputter coating. The fractured sample was coated with a thin layer (~10 nm) of platinum, a conductive material, to reduce charging during imaging. The preparation and SEM cryo-stage temperature was set at −140 °C, and the anti-contaminator temperature was fixed at −175 °C. The key settings for all cryo-SEM micrographs were similar, and the original micrographs with accompanying settings and their corresponding EDS maps can be found in the ESI.† The surface topography of the samples was imaged using a secondary electron secondary ion (SESI) detector. The electron high tension (EHT) fixed the acceleration voltage at 5 kV, which was appropriate for EDS detection. The working distance was set at ≈5 mm. The probe current for Fig. 4(d) was 50 pA and for all other micrographs was 100 pA.

The cryo-SEM is combined with an Oxford Instruments X-Max^N 150 EDS detector. EDS measures the characteristic X-rays emitted due to interactions between the electron beam and atoms in the sample so as to identify elements and quantify their abundance. For our samples, EDS analysis confirms the presence of carbon (C), oxygen (O), fluorine (F), silicon (Si), and others. By comparing with the main components in our mixed foams, the regions occupied by a majority of C, O, F, and Si are, respectively, taken to represent the oil phase, aqueous phase, fluorinated particles, and silica particles. In all the multi-coloured EDS overlays, the oil phase, the aqueous phase, the fluorinated particles, and the silica particles are coloured light blue, orange, dark blue, and pink, respectively. Quantifying how the elemental composition varies across a linear path on the sample surface is achieved *via* a line scan. Several parallel line scans (spaced 1 μm apart) were taken and integrated together to improve the statistics. For linear analysis data, the aqueous and oil phases are distinguished by the amount of oxygen and carbon. We define the intersection points of the counts of carbon and oxygen to represent the positions of the oil–aqueous interfaces. The EDS analysis is quantitative; however, it can be impacted by sample topography including surface roughness, surface defects, and local inclinations.[33,34] Due to these effects we are not able to quantify the elemental composition of the sample, only indicate what elements may be present and where. The binning factor for all the EDS data is two. To smooth the line scan graphs, five adjacent counts are averaged together.

Fig. 2 shows two O/W samples with different propylene glycol concentrations, the aqueous to oil foam mass ratio is fixed at 1 : 1. By comparing the cryo-SEM micrographs (Fig. 2(a) and (c)) to their EDS maps (Fig. 2(b) and (d)), obviously the oil and aqueous phases can be easily distinguished from the aqueous–oil interfaces. For the sample containing half propylene glycol in the aqueous phase, the cryo-SEM micrograph and

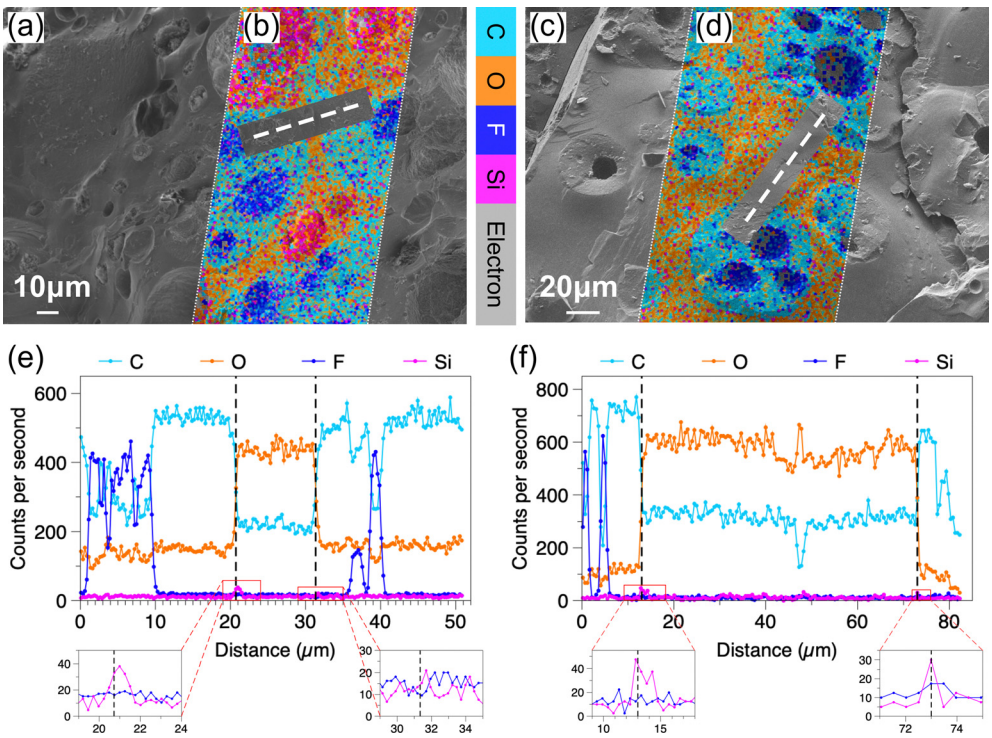

Fig. 2 (a) and (c) Cryo-SEM micrographs and their corresponding (b) and (d) EDS maps for O/W mixed foams. The multi-coloured layered map shows oil phase (light blue), aqueous phase (orange), fluorinated particles (dark blue), and silica particles (pink). The aqueous to oil foam mass ratio is (a)–(d) 1 : 1. The propylene glycol volume fractions in the aqueous phase are (a) and (b) 1/2 and (c) and (d) 9/14. (e) and (f) EDS analyses along the linescans shown on (b) and (d), respectively. The linescan lengths in (b) and (d) are 50.9 μm and 82.7 μm, respectively.

EDS map (Fig. 2(a) and (b)) look consistent with its confocal micrograph (Fig. 1(i)). Droplets similar to multiple emulsions randomly emerge in the mixed foams, and here a W/O/W droplet is caught (top right corner in Fig. 2(b)). The positions of the line scans in Fig. 2(e) and (f) are highlighted by the dashed lines shown in Fig. 2(a) and (c), respectively. In Fig. 2(e), from left to right, the line scan starts from a fluorinated-particle-stabilised bubble in an oil foam droplet, passing through the aqueous phase in-between two aqueous–oil interfaces, and finally ends in another oil foam droplet. Between 0–10 μm and 35–41 μm, the appearance of oil bubbles is represented by the fluctuating F counts (dark blue) along with a simultaneous significant drop of C counts (light blue) and a small decrease of O counts (orange). If any aqueous region is detected, the counts of C and O will show opposite behaviour; meanwhile, the fluctuation of F will be replaced by that of Si. According to the crossing points of C and O counts, two aqueous–oil interfaces can be identified. Here we note that a Si peak appears to accompany the interface, just like the left interface in Fig. 2(e). An interface without this kind of Si peak is not commonly observed, and the right interface in Fig. 2(e) is an extremely rare example. Minor silica particle deficiency appears not to cause sample instability. Similar stable partially covered droplets have previously been observed in simple Pickering emulsions.[35] By contrast, the counts of F are always independent of the oil–aqueous interface. When the propylene glycol volume fraction increases to 9/14, the small population of aqueous bubbles shown in the confocal micrograph (Fig. 1(g)) is not then observed during cryo-SEM (Fig. 2(c) and (d)). This difference could be due to the fracture trajectory or might be the result of rapid freezing. In Fig. 2(f), two Si peaks appear when the line scan in Fig. 2(d) crosses the liquid–liquid interface. Again, the only fluctuation of F counts happens upon encountering the bubble in the oil.

Fig. 3 presents results for the W/O mixed foam sample with 1/2 propylene glycol in the aqueous phase; the aqueous to oil mass ratio is 2 : 3. Its EDS map (Fig. 3(a)) and cryo-SEM micrograph (Fig. 3(b)) show the same morphology as its confocal micrograph (Fig. 1(m)). The line scan in Fig. 3(b) across the liquid–liquid interfaces does not pass through any bubbles; hence, there are no large fluctuations for Si and F counts in Fig. 3(c). There are two Si peaks corresponding to the aqueous droplet interfaces. Fig. 3(d) shows the counts *versus* distance determined by averaging 24 horizontal parallel lines that were uniformly distributed in the rectangular box in Fig. 3(e). Each single line scan was shifted to convert the arc-shaped droplet interface to a straight line with the aqueous–oil interface aligned. The error bar is the standard error. The pink Si peak in the 3–8 μm graph verifies that the silica particles are overlapped with the aqueous–oil interface. Conversely, there is no observable peak related to the fluorinated particles at this interface. Between 7 and 12 μm, the dark blue F peak with distinct error bars corresponds to the bubble in the oil phase that appears in the middle of the bottom in the rectangular box. After 12 μm, the counts of C and O cross again. However, as the multiple lines have been aligned based on the droplet interface

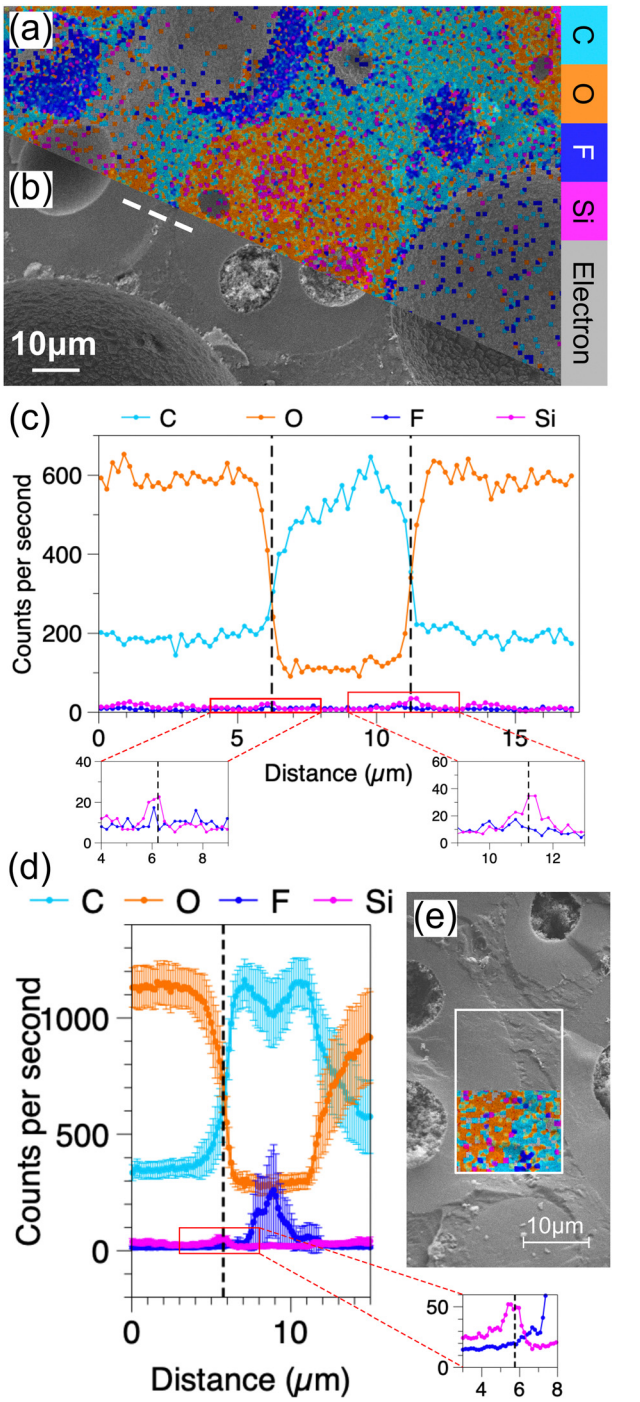

Fig. 3 (a) EDS map and its corresponding (b) cryo-SEM micrograph for a W/O mixed foam. The multi-colored layered map shows the oil phase (light blue), aqueous phase (orange), fluorinated particles (dark blue), and silica particles (pink). The aqueous to oil foam mass ratio is 2 : 3. The propylene glycol volume fraction in the aqueous phase is 1/2. (c) EDS analysis is performed following the linescan shown in (b). The linescan length is 17.1 μm. (d) 24 parallel EDS linescans (16.5 μm) are evenly distributed in the rectangular area shown in (e). EDS analyses are averaged after aligning the linescans based on the position of the aqueous–oil interface in (e) (the boundary that separates the orange and light blue regions).

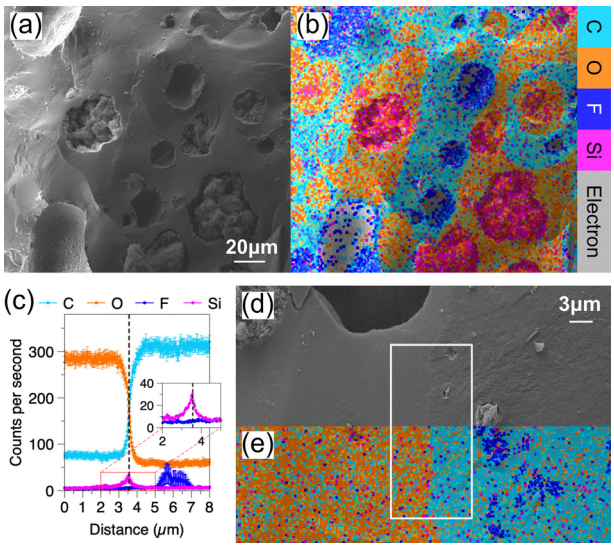

Fig. 4 (a) Cryo-SEM micrograph and its corresponding (b) EDS map for a phase-separated mixed foam. The multi-colored layered map shows the oil phase (light blue), aqueous phase (orange), fluorinated particles (dark blue), and silica particles (pink). The aqueous to oil foam mass ratio is 1 : 1. The propylene glycol volume fraction in the aqueous phase is 5/14. (c) Averaged EDS analyses of 24 parallel EDS linescans (10.6 μm) that are evenly distributed in the rectangular area are shown in (d). The linescans are aligned based on the position of the aqueous–oil interface in (d) and (e) (the boundary that separates the orange and light blue regions).

around 5.8 μm, the error bars corresponding to C and O are much larger than those in the previous region. Additionally, any existing maximum of the Si counts is hidden due to the data being mis-aligned.

For the phase-separated sample, its heterogeneous structure captured by cryo-SEM (Fig. 4(a)) and EDS (Fig. 4(b)) is consistent with its confocal micrograph (Fig. 1(k)). Both the O/W and W/O regions exist simultaneously, and W/O/W and O/W/O droplets can be found distributed at random. Its aqueous to oil foam mass ratio is 1 : 1, and the propylene glycol volume fraction in the aqueous phase is 5/14. The counts in Fig. 4(c) are the average from 24 linescans that are evenly distributed in the white rectangle box (Fig. 4(d) and (e)). The linescans are aligned using the same relocation method used for Fig. 3(d). The location of the sharp Si peak is highly consistent with that of the boundary between the aqueous and oil phases. The peak of F counts between 5 and 7 μm is caused by two defects within the oil phase (top right in the rectangular box in Fig. 4(d)). Elsewhere, the counts of F remain at a low value. By freezing the phase-separated sample a few hours after preparation, an obvious silicon layer, which is overlapping entirely with the surface of an aqueous droplet is directly observed from the EDS map (see Fig. S5 in the ESI†). This unique layer has not been found within the other samples. The most likely reason is that the aqueous liquid can easily drain out from this most unstable sample, and W/O regions come to dominate the phase-separated sample gradually. If the bubbles are disrupted during this process, the silica particles might aggregate at the aqueous–oil interfaces. Nonetheless we cannot rule out inaccuracies caused by differences in surface roughness.

Here we have demonstrated that cryo-SEM and EDS studies make it possible to resolve outstanding questions about composite soft materials. Specifically for mixed foam samples we have shown that aqueous–oil interfaces are almost always associated with the presence of silica particles. It is less clear whether the silica particle coating is uniform and also if it is dependent on the morphology of the samples. A crucial factor that affects the EDS measurements is the surface topography of the fractured samples. While all the samples were fractured carefully and are locally flat and smooth, the similarity between them is still not well controlled. Therefore, comparing the trends of element counts between different samples rather than their exact values is more credible. Overall, the variation of fluorine counts is independent of the location of the aqueous–oil interfaces, whereas the tiny but appreciable silicon peaks corresponding to the aqueous–oil interfacial positions indicate that silica particles are critical for liquid–liquid interface stabilisation. We note that it is likely that the viscoelastic properties of the mixed foams also play a role in their overall stability.

Author contributions

YS carried out the investigation directed on SEM measurements by FHJL. Supervision was by TL and PSC. The project conceptualisation was by PSC. Writing – the original draft was by YS and PSC. Writing, reviewing and editing were carried out by all authors.

Conflicts of interest

There are no conflicts to declare.

Acknowledgements

We are grateful for financial support from the EPSRC (EP/P030564/1). For the purpose of open access, the authors have applied a Creative Commons Attribution (CC BY) licence to any Author Accepted Manuscript version arising from this submission.

Notes and references

1 C. Hill and J. Eastoe, *Adv. Colloid Interface Sci.*, 2017, **247**, 496–513.
2 M. Chappat, *Colloids Surf., A*, 1994, **91**, 57–77.
3 L. L. Schramm, *Emulsions, foams, and suspensions: fundamentals and applications*, John Wiley & Sons, 2006.
4 E. Rio, W. Drenckhan, A. Salonen and D. Langevin, *Adv. Colloid Interface Sci.*, 2014, **205**, 74–86.
5 T. N. Hunter, R. J. Pugh, G. V. Franks and G. J. Jameson, *Adv. Colloid Interface Sci.*, 2008, **137**, 57–81.
6 S. Damodaran, *J. Food Sci.*, 2005, **70**, R54–R66.
7 L. Gilbert, C. Picard, G. Savary and M. Grisel, *Colloids Surf., A*, 2013, **421**, 150–163.
8 Y. Chevalier and M.-A. Bolzinger, *Colloids Surf., A*, 2013, **439**, 23–34.

9 R. Aveyard, B. P. Binks and J. H. Clint, *Adv. Colloid Interface Sci.*, 2003, **100**, 503–546.
10 U. T. Gonzenbach, A. R. Studart, E. Tervoort and L. J. Gauckler, *Langmuir*, 2006, **22**, 10983–10988.
11 A. Ding, B. P. Binks and W. A. Goedel, *Langmuir*, 2005, **21**, 1371–1376.
12 E. Read, S. Fujii, J. Amalvy, D. Randall and S. Armes, *Langmuir*, 2004, **20**, 7422–7429.
13 M. Yekeler, U. Ulusoy and C. Hiçylmaz, *Powder Technol.*, 2004, **140**, 68–78.
14 A. San-Miguel and S. H. Behrens, *Langmuir*, 2012, **28**, 12038–12043.
15 B. P. Binks, P. D. Fletcher, B. L. Holt, P. Beaussoubre and K. Wong, *Phys. Chem. Chem. Phys.*, 2010, **12**, 11954–11966.
16 B. P. Binks, P. D. Fletcher, M. A. Thompson and R. P. Elliott, *Langmuir*, 2013, **29**, 5723–5733.
17 T. S. Horozov, *Curr. Opin. Colloid Interface Sci.*, 2008, **13**, 134–140.
18 B. P. Binks, A. Rocher and M. Kirkland, *Soft Matter*, 2011, **7**, 1800–1808.
19 Y. Si, T. Li and P. S. Clegg, *Langmuir*, 2022, **38**, 4243–4249.
20 Y. Si, J. R. Royer, T. Li and P. S. Clegg, *J. Colloid Interface Sci.*, 2023, **646**, 671–678.
21 B. P. Binks and R. Murakami, *Nat. Mater.*, 2006, **5**, 865–869.
22 B. P. Binks and B. Vishal, *Adv. Colloid Interface Sci.*, 2021, **291**, 102404.
23 A. Salonen, *Curr. Opin. Colloid Interface Sci.*, 2020, **50**, 101381.
24 X. Gu, J. Guo and Z. Meng, *Food Hydrocolloids*, 2023, **144**, 109000.
25 S. H. Behrens, *Curr. Opin. Colloid Interface Sci.*, 2020, **50**, 101384.
26 N. Yan, M. R. Gray and J. H. Masliyah, *Colloids Surf., A*, 2001, **193**, 97–107.
27 B. Binks and S. Lumsdon, *Langmuir*, 2000, **16**, 2539–2547.
28 B. Binks and S. Lumsdon, *Langmuir*, 2000, **16**, 3748–3756.
29 B. P. Binks, J. Philip and J. A. Rodrigues, *Langmuir*, 2005, **21**, 3296–3302.
30 J. Sjöblom, *et al.*, *Emulsions and emulsion stability*, Taylor & Francis, New York, NY, USA, 2006, vol. 45.
31 Y. Liu, E. L. Carter, G. V. Gordon, Q. J. Feng and S. E. Friberg, *Colloids Surf., A*, 2012, **399**, 25–34.
32 E. Guo, G. Zeng, D. Kazantsev, P. Rockett, J. Bent, M. Kirkland, G. Van Dalen, D. S. Eastwood, D. StJohn and P. D. Lee, *RSC Adv.*, 2017, **7**, 15561–15573.
33 T. Rönnhult, B. Brox and G. Fritze, *Scanning*, 1987, **9**, 81–87.
34 D. E. Newbury and N. W. Ritchie, *Scanning*, 2013, **35**, 141–168.
35 E. Vignati, R. Piazza and T. P. Lockhart, *Langmuir*, 2003, **19**, 6650–6656.